Effect of Internal Interfaces on Hardness and Thermal Stability of Nanocrystalline $Ti_{0.5}Al_{0.5}N$ Coatings

D. RAFAJA, C. WÜSTEFELD, C. BAEHTZ, V. KLEMM, M. DOPITA, M. MOTYLENKO, C. MICHOTTE, and M. KATHREIN

The effect of microstructure on the thermal stability and hardness of the cathodic arc evaporated $Ti_{0.5}Al_{0.5}N$ coatings was investigated with the aid of the *in-situ* high-temperature X-ray diffraction experiments, which were accompanied by high-resolution transmission electron microscopy (HRTEM) and nanoindentation measurements. The microstructure of the coatings was modified through the choice of the bias voltage in the deposition process. It was found that the bias voltage affects strongly the uniformity of the local distribution of titanium and aluminum in the coatings. The nonuniform distribution of the elements contributes to the formation of lattice strains at the crystallite and phase boundaries. The lattice strains at the crystallite boundaries increase the hardness of the coatings; the lattice strains at the phase boundaries improve their thermal stability. A certain nonuniformity of the distribution of the metallic species in the coatings is regarded as advantageous. However, a great nonuniformity in the distribution of the metallic species accelerates the degradation of the coatings at high temperatures. As a measure for the nonuniformity of the distribution of the atomic species in the as-deposited (Ti, Al) N samples, the stress-free lattice parameter of fcc-(Ti, Al) N is suggested.

DOI: 10.1007/s11661-010-0204-8
© The Minerals, Metals & Materials Society and ASM International 2010

I. INTRODUCTION

A good thermal stability of hard protective coatings is a very important issue, particularly if the coatings are intended for use in machining applications at high cutting speeds or for dry cutting.[1] For such "high-temperature" applications, several advantages of nanocrystalline hard coatings based on the titanium aluminum nitride are used. The prominent examples of the beneficial properties of the (Ti, Al) N coatings at high temperatures are their excellent oxidation resistance (*e.g.*, References 2 through 4) and the increase of their hardness after thermal loading up to approximately 1223 K (950 °C).[5,6] The frequently reported phenomena, which negatively influence the hardness of the (Ti, Al) N coatings at high temperatures, are the relaxation of the compressive residual stresses[4,7–11] and the decomposition of the metastable supersaturated (Ti, Al) N having the fcc crystal structure into fcc-(Ti, Al) N with lower aluminum contents and into wurtzitic w-AlN.[12] Moreover, as the hardness of the nanocrystalline coatings typically increases with decreasing crystallite size[13] according to the Hall–Petch relationship[14,15] and as it reaches its maximum at the crystallite sizes of 3 to 4 nm (in the case of the fcc-(Ti, Al) N crystallites, *e.g.*, References 16 through 18), the growth of crystallites at high temperatures can be regarded as an additional factor, which reduces the hardness of the coatings at high temperatures.

In our previous publications,[17–19] we have shown that the hardness of the as-deposited, nonannealed (Ti, Al) N nanocrystalline coatings and thin film nanocomposites is controlled by an interplay of several microstructural features such as phase composition, mutual crystallographic orientation of adjacent crystallites (particularly at the phase boundaries), lattice misfit, lattice strain, and the formation of defect structures. From this point of view, the presence of the minor w-AlN separating fcc-(Ti, Al) N nanocrystallites from each other was regarded as a factor increasing the hardness of the (Ti, Al) N nanocomposites. In general, the phase composition of the (Ti, Al) N nanocrystalline coatings is driven by the aluminum contents.[5,11,20–22] However, there is a remarkable spread in the reported solubility limits of Al in fcc-(Ti, Al) N. This was already concluded by PalDey and Deevi,[23] who related the maximum concentration of aluminum in fcc-(Ti, Al) N to the deposition conditions. Recently, the bias voltage was discussed to be a factor influencing the phase composition of the as-deposited Ti-Al-X-N coatings with X = Ta and V (References 24 and 25). In Reference 26, it was shown that even the distribution of Al in the microstructure of

D. RAFAJA, Professor of Structure Research, C. WÜSTEFELD, Postdoctoral Student, V. KLEMM, Head of TEM Laboratory, M. DOPITA, Postdoctor, and M. MOTYLENKO, Postdoctoral Student, are with the Institute of Materials Science, TU Bergakademie Freiberg, D-09599 Freiberg, Germany. Contact e-mail: rafaja@ww.tu-freiberg.de C. BAEHTZ, Beamline Scientist, is with the Institute of Ion Beam Physics and Materials Research, Forschungszentrum Dresden-Rossendorf, Bautzner Landstrasse 400, D-01328 Dresden, Germany. C. MICHOTTE, Application Engineer, is with the Ceratizit Luxembourg S.à.r.l., Route de Holzem, 101, B.P. 51, L-8201 Mamer, Luxembourg. M. KATHREIN, Head of Physical Surface Engineering, is with Ceratizit Austria GmbH, A-6600 Reutte, Austria.

Manuscript submitted December 11, 2009.
Article published online March 30, 2010

the (Ti, Al) N coatings can affect the phase stability of supersaturated fcc-(Ti, Al) N. Another important issue is the effect of the strain and surface energy on the phase stability[27] and on the energetic balance of the decomposition process.[28]

The main aims of this contribution are description and explanation of the correlation between the microstructure of as-deposited coatings, the microstructural changes and hardness variations at high temperatures, and the thermal stability of the coatings. The subjects of the study were $Ti_{0.5}Al_{0.5}N$ coatings with different microstructures in the as-deposited state, which were deposited using cathodic arc evaporation (CAE) at two different bias voltages, $U_B = -40$ V and $U_B = -80$ V. The microstructure analysis of the as-deposited coatings was performed using a combination of glancing-angle X-ray diffraction (GAXRD) and high-resolution transmission electron microscopy (HRTEM). The goals of the microstructure analysis were the quantification of the phase composition in the coatings, the determination of the orientation relationship between adjacent phases, and the determination of the resulting lattice strains. The development of these microstructural parameters at high temperatures was investigated by *in-situ* high-temperature–glancing-angle X-ray diffraction (HT-GAXRD) measurements, which were carried out at gradually increasing temperatures. In order to be able to follow the effect of the spinodal decomposition[29] on the preceding microstructural parameters, the samples were cooled to approximately 373 K (100 °C) after each temperature exposure. Furthermore, this temperature profile helped us to separate the decomposition-related microstructural phenomena from the effects of the thermal expansion.

II. EXPERIMENTAL DETAILS

The $Ti_{0.5}Al_{0.5}N$ coatings were deposited in an industrial scale CAE facility of the Balzers RCS type[30,31] from cathodes containing 50 at. pct Ti and 50 at. pct Al. Nitrogen with the pressure of 3.2×10^{-2} mbar was used as the working atmosphere. The deposition was performed at 723 K (450 °C); the bias voltage was −40 and −80 V for the respective sample series. As substrates, cemented carbide SNUN type cutting inserts (grade S40T) were used.

The as-deposited coatings were analyzed by means of electron probe microanalysis with wavelength-dispersive X-ray spectroscopy (EPMA/WDS), glow discharge optical emission spectroscopy (GDOES), GAXRD, and HRTEM. EPMA/WDS was used to verify the stoichiometric ratios of the metallic species in the coatings, *i.e.*, [Al]/([Ti] + [Al]) and [Ti]/([Ti] + [Al]). The EPMA/WDS measurements were performed on a JXA 8900 RL from JEOL.* GDOES was employed to check the nitrogen contents in the coatings. These experiments were performed on a Spectru-Mat 750 from LECO.** GAXRD was expected to yield information about the phase composition of the as-deposited coatings and, for the fcc phase, about the stress-free lattice parameters, the residual stresses, and the crystallite size. HRTEM was used to verify the phase composition and the crystallite size that was obtained from the GAXRD measurements, to assign the crystal structure of bits of aluminum nitride found in some samples, and to determine the orientation relationship between fcc-(Ti, Al) N and AlN at their interfaces.

The laboratory GAXRD experiments on the as-deposited samples were performed using a D8 Advance diffractometer (from Bruker AXS) that was equipped by a sealed X-ray tube with copper anode, by a Goebel mirror located in the primary beam, and by a Soller collimator with the acceptance of 0.12 deg and a flat LiF monochromator located in front of a scintillation detector. The LiF monochromator reduced the Cu $K_{\alpha 2}$/Cu $K_{\alpha 1}$ intensity ratio to 0.08. The angle of incidence of the primary beam on the sample surface was set to 3 deg. HRTEM was done on a 200 kV analytical high-resolution transmission electron microscope JEM 2010 FEF (from JEOL), which was equipped with an ultrahigh resolution objective lens (C_s = 0.5 mm) and an in-column energy filter. The in-column filter improves the quality of the HRTEM micrograph by removing the in-elastically scattered electrons from the image.

Changes in the microstructure of the coatings at high temperatures were investigated by *in-situ* high-temperature XRD experiments that were performed at the Rossendorf Beamline (ROBL) at ESRF in the GAXRD mode at the wavelength of 0.08857 nm and at the angle of incidence of the primary beam on the sample surface of 0.5 deg. For the *in-situ* synchrotron HT-GAXRD measurements, a substantially smaller glancing angle was selected than for the laboratory measurements in order to keep the penetration depth of X-rays approximately the same as for the laboratory GAXRD experiments. The *in-situ* HT-GAXRD measurements were done at gradually increasing temperatures, as shown in Figure 1. As a part of the microstructural changes was expected to be driven by the spinodal decomposition, one GAXRD measurement at approximately 373 K (100 °C) followed each HT-GAXRD experiment excepting the measurement at 723 K (450 °C) (Figure 1). The heating of the samples prior to the HT-GAXRD measurement took approximately 30 minutes, each measurement 60 minutes, and the cooling 30 minutes. After the HT-GAXRD measurement done at 723 K (450 °C), the samples were not cooled. As the coatings were deposited at approximately 723 K (450 °C), no microstructural changes were expected at this temperature. All *in-situ* HT-GAXRD experiments were carried out in vacuum; the pressure in the high-temperature chamber was about 10^{-5} mbar.

*JEOL is a trademark for Japan Electron Optics Ltd., Tokyo.

**LECO is a trademark of LECO Corporation, St. Joseph, MI.

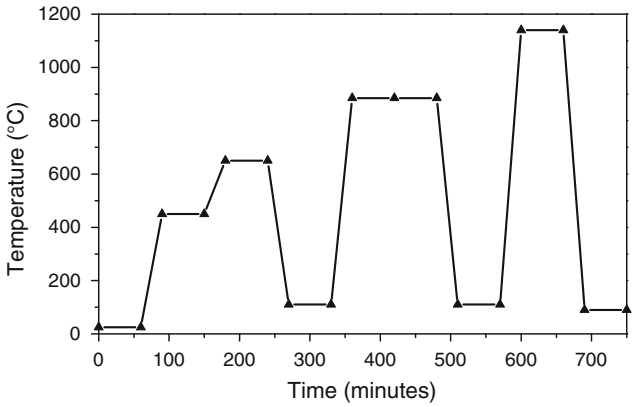

Fig. 1—Temperature profile on the samples as used for *in-situ* HT-GAXRD measurements. The triangles mark the start and the end of the respective measurements.

III. RESULTS

A. *Phase Composition of As-Deposited Coatings*

The crucial microstructure parameter influencing the hardness of (Ti, Al) N coatings is their phase composition (References 17 through 19). Frequently, the phase composition is concluded directly from the presence or absence of diffraction lines of the respective phase in the XRD patterns. However, this method of phase analysis fails in many cases, for instance, if the relative volume of one crystalline phase is below the detection limit of XRD, if one of the phases contains a very high density of microstructure defects, or if the diffraction lines overlap because of the match of the interplanar spacing. As an auxiliary method for the phase analysis on the (Ti, Al) N nanocrystalline coatings and thin film nanocomposites, the comparison of the measured stress-free lattice parameter with the lattice parameter as expected for the respective chemical composition of the coating was recommended in References 17 and 19. For fcc-$Ti_{1-x}Al_xN$, the "expected" stress-free lattice parameter can be calculated from the Vegard-like dependence.[19]

$$a = [0.42418(2) - 0.01432(2)\cdot x] \text{ nm} \qquad [1]$$

The function of this procedure can be illustrated on the CAE $Ti_{0.5}Al_{0.5}N$ coatings deposited at $U_B = -40$ and -80 V. In the XRD patterns of both samples (Figure 2), only reflections from fcc-(Ti, Al) N (coating) and WC (substrate) are visible. Neither the diffraction lines from w-AlN nor from fcc-AlN could be found. Thus, the XRD patterns were subjected to line profile fitting in order to obtain exact positions of the diffraction lines and their widths for further analyses. The first indicator of differences in the microstructure of the $Ti_{0.5}Al_{0.5}N$ coatings deposited at different bias voltages is the different dependence of the lattice parameters of fcc-(Ti, Al) N on $\sin^2\psi$ (Figure 3).[33,34] The lattice parameters are calculated from the positions of XRD lines; ψ is the angle between the diffracting lattice planes and the sample surface. For GAXRD, ψ is equal to the difference between half of the diffraction angle (θ) and the angle of incidence of the primary beam on the sample surface (γ), $\psi = \theta - \gamma$. It can be seen from Figure 3 that the lattice parameters are higher and the slope of the a *vs* $\sin^2\psi$ plot is steeper in the coating deposited at $U_B = -80$ V than in the coating deposited at $U_B = -40$ V. From the linear dependence of the lattice parameters on $\sin^2\psi$,[33,34]

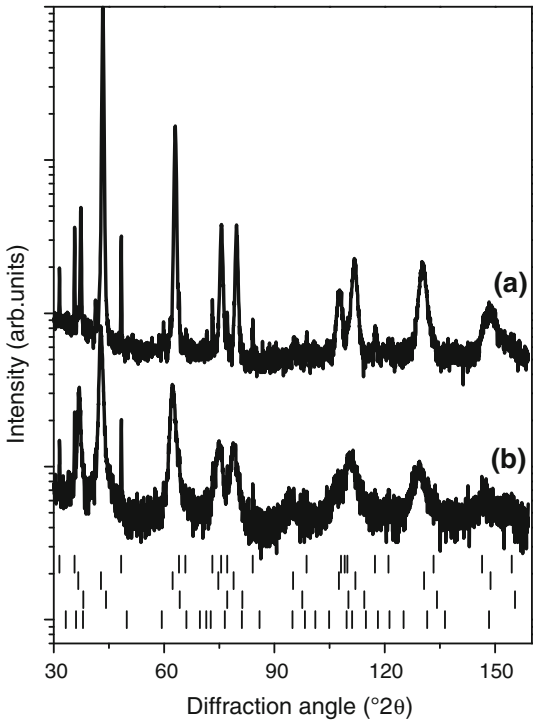

Fig. 2—X-ray diffraction patterns of the CAE $Ti_{0.5}Al_{0.5}N$ coatings deposited at (*a*) $U_B = -40$ V and (*b*) $U_B = -80$ V. The line position marks are for hexagonal WC (substrate),[32] fcc-$Ti_{0.5}Al_{0.5}N$,[19] fcc-AlN (high-pressure phase from Reference 32), and w-AlN[32] (from the top to the bottom). These measurements were carried out on a laboratory X-ray diffractometer using Cu K_α radiation.

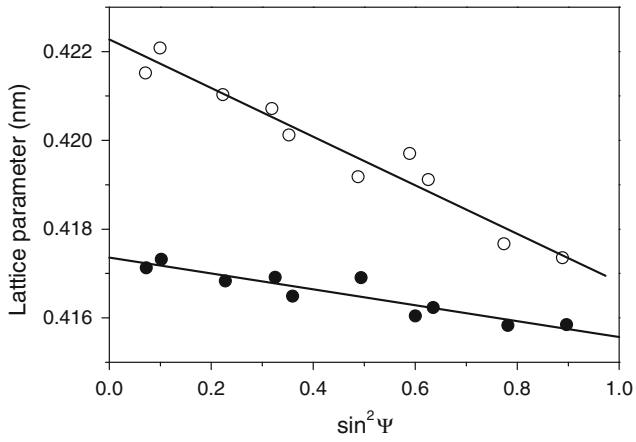

Fig. 3—Dependence of the lattice parameters on $\sin^2\psi$, as obtained for the CAE $Ti_{0.5}Al_{0.5}N$ coatings deposited at $U_B = -40$ V (solid symbols) and $U_B = -80$ V (open symbols). The solid lines are the linear fits according to Eq. [2] that were used for calculation of the stress-free lattice parameters, lattice strains, and residual stresses summarized in Table I.

$$a = a_{\perp} + (a_{||} - a_{\perp}) \sin^2 \psi \quad [2]$$

the out-of-plane ($a_{\perp}$) and the in-plane ($a_{||}$) lattice parameters were calculated. These quantities were further used for calculation of the stress-free lattice parameter,

$$a_0 = a_{\perp} + \frac{2\nu}{\nu + 1}(a_{||} - a_{\perp}) \quad [3]$$

for calculation of the "macroscopic" lattice strain caused by the residual stress,[35]

$$\varepsilon = \frac{a_{||} - a_{\perp}}{2a_0} \quad [4]$$

and for calculation of the residual stress itself:

$$\sigma = \frac{a_0 - a_{\perp}}{a_0} \cdot \frac{E}{2\nu} \quad [5]$$

The values of the preceding parameters are summarized in Table I, as calculated for the Poisson ratio $\nu = 0.3$ and for the Young modulus $E = 500$ GPa.[36] Although the Young's modulus of the samples was verified by nanoindentation measurements, the value of the residual stress is still much less reliable than the value of the macroscopic lattice strain, which is determined almost directly from the XRD data. The only parameter that is needed to calculate the stress-free lattice parameter and the macroscopic lattice strain is the Poisson ratio (Eqs. [2] through [4]).

Within the experimental accuracy, the stress-free lattice parameter of the $Ti_{0.5}Al_{0.5}N$ coating deposited at $U_B = -40$ V (filled circle in Figure 4) agrees with the lattice parameter calculated from Eq. [1] for $x = 0.5$ (solid line in Figure 4). The high stress-free lattice parameter of the $Ti_{0.5}Al_{0.5}N$ coating deposited at $U_B = -80$ V (open circle in Figure 4) indicates that the fcc-(Ti, Al) N phase present in the sample contains less aluminum than corresponds to the overall chemical composition [Ti]/([Ti] + [Al]) = 0.5. A possible explanation is that aluminum, which is missing in fcc-(Ti, Al) N, forms another phase.[17] According to Eq. [1], the stress-free lattice parameter $a_0 = (0.4198 \pm 0.0002)$ nm measured in the $Ti_{0.5}Al_{0.5}N$ coating deposited at $U_B = -80$ V (Table I) corresponds to the aluminum contents of 31 at. pct in the fcc phase, *i.e.*, $Ti_{(0.69\pm0.02)}Al_{(0.31\pm0.02)}N$ (*cf.* Figure 4). Assuming that the other phase in the sample is aluminum nitride, the phase composition of this coating can be estimated to be (72 ± 2) mol pct fcc-$Ti_{(0.69\pm0.02)}Al_{(0.31\pm0.02)}N$ and (28 ± 2) mol pct AlN.

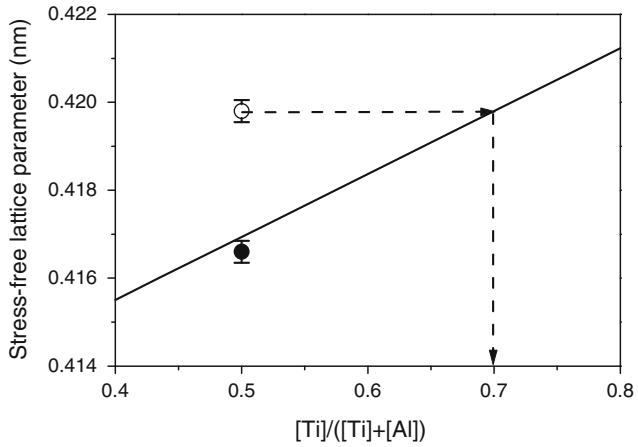

Fig. 4—Comparison of the stress-free lattice parameters from Table I with the Vegard-like dependence from Eq. [1]. The Vegard-like dependence of the stress-free lattice parameter on the [Ti]/([Ti] + [Al]) ratio in the coatings is plotted by the solid line. The symbols represent the stress-free lattice parameters of the coatings deposited at $U_B = -40$ V (solid circle) and $U_B = -80$ V (open circle). According to Eq. [1], the lattice parameter of (0.4198 ± 0.0002) nm corresponds to [Ti]/([Ti] + [Al]) = (0.69 ± 0.02) in fcc-$Ti_{1-x}Al_xN$.

The presence of AlN in the coating deposited at $U_B = -80$ V was confirmed by the fast fourier transformation (FFT) of selected regions in the HRTEM micrographs (Figure 5). From the interplanar spacings and from the angles between the lattice planes obtained from the FFT/HRTEM patterns (insets in Figure 5), it could be concluded that this coating contains fcc-(Ti, Al) N, as already proven by XRD, and w-AlN. In addition, the analysis of the FFT/HRTEM patterns revealed the following orientation relationship between fcc-(Ti, Al) N and w-AlN at their interfaces: $[1\bar{1}0]_{TiN} || [10\bar{1}0]_{AlN}$ (both vectors lie in the direction of the primary electron beam) and $(\bar{1}\bar{1}1)_{TiN} || (0002)_{AlN}$ (the normal vectors to the lattice planes lie in the plane of the HRTEM micrograph). The lattice misfit calculated for this orientation relationship between fcc-(Ti, Al) N and w-AlN and for the lattice parameters $a = 0.4198$ nm (measured stress-free lattice parameter of fcc-(Ti, Al) N; Table I and Figure 4) and $a = 0.3111$ nm and $c = 0.4978$ nm (lattice parameters of w-AlN taken from Reference 32) is equal to

$$\varepsilon_1 = 2 \cdot \frac{a(\mathrm{w}) - a(\mathrm{fcc})/\sqrt{2}}{a(\mathrm{w}) + a(\mathrm{fcc})/\sqrt{2}} \approx 0.047 \quad [6]$$

along the $[1\bar{1}0]_{TiN} || [10\bar{1}0]_{AlN}$ direction and

Table I. Basic Structural and Mechanical Characteristics of the Thin Films

Characteristics	$U_B = -40$ V	$U_B = -80$ V
Stress-free lattice parameter, a_0	(0.4165 ± 0.0002) nm	(0.4198 ± 0.0003) nm
Macroscopic lattice strain, ε	$-(2.1 \pm 0.3) \times 10^{-3}$	$-(6.5 \pm 0.5) \times 10^{-3}$
Residual stress, σ	−(1.7 ± 0.2) GPa	−(5.0 ± 0.4) GPa
Crystallite size	(6.9 ± 0.5) nm	(4.0 ± 0.2) nm
Hardness, H_{IT}	(29.7 ± 0.8) GPa	(34.2 ± 0.9) GPa

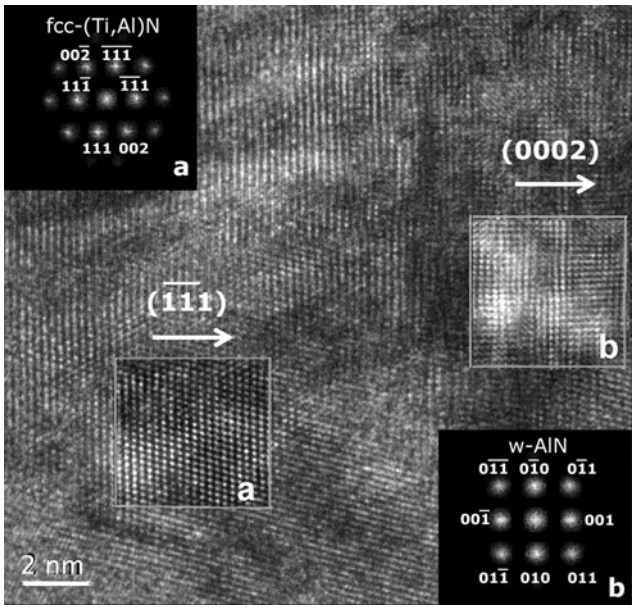

Fig. 5—HRTEM micrograph of an interface between fcc-(Ti, Al) N (region *a*) and w-AlN (region *b*) taken in the coating deposited at $U_B = -80$ V. The assignments of the phases and their mutual orientation relationships were performed with the aid of the FFT/HRTEM patterns (insets).

$$\varepsilon_2 = 2 \cdot \frac{c(\mathrm{w})/2 - a(\mathrm{fcc})/\sqrt{3}}{c(\mathrm{w})/2 + a(\mathrm{fcc})/\sqrt{3}} \approx 0.027 \qquad [7]$$

as calculated from the difference in the interplanar spacings d_{0002}(w-AlN) and d_{111}(fcc-(Ti, Al) N). In both cases, the lattice misfit is positive. This means that the current orientation relationship between fcc-(Ti, Al) N and w-AlN and the preceding lattice parameters of these phases cause an expansion of the elementary cell of fcc-(Ti, Al) N and a compression of the elementary cell of w-AlN. The lattice expansion of fcc-(Ti, Al) N could cause compressive residual stress in this phase, if the in-plane expansion of the fcc-(Ti, Al) N crystallites is constrained by the adhesion of the coating to the substrate[37] or if the fcc-(Ti, Al) N/w-AlN interfaces form preferentially in the perpendicular direction to the substrate. Another possible result of the lattice misfit between fcc-(Ti, Al) N and w-AlN is an inhomogeneous local lattice deformation that is responsible for a part of the XRD line broadening, as discussed later in this section. Because of the dependence of the stress-free lattice parameter in fcc-$Ti_{1-x}Al_xN$ on the aluminum contents (Eq. [1]), the lattice misfit between fcc-(Ti, Al) N and w-AlN decreases if Al segregates from fcc-(Ti, Al) N (Eqs. [6] and [7]). However, the lattice misfit at the fcc-(Ti, Al) N/w-AlN interfaces is not the sole source of residual stresses. A certain level of the intrinsic residual stress was already observed in the single-phase $Ti_{0.5}Al_{0.5}N$ coating deposited at $U_B = -40$ V (Table I).

The XRD line broadening (Figure 6) shows features that are frequently observed in compact nanocrystalline materials,[17–19,34] *i.e.*, an increase at low diffraction vectors and almost no change at high diffraction vectors. The reason for such departure from the well-known

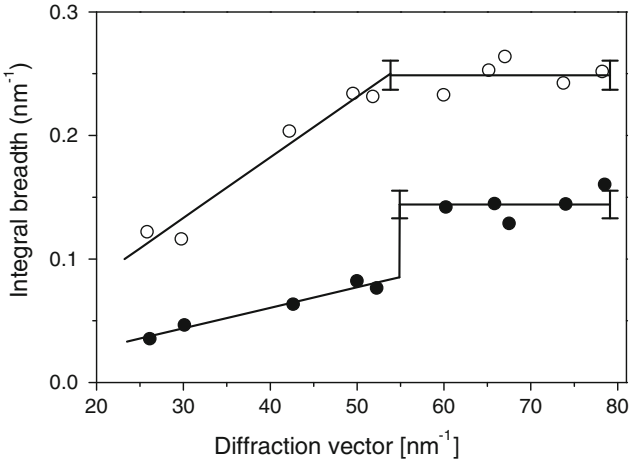

Fig. 6—Dependence of the integral breadth of XRD lines on the modulus of the diffraction vector ($4\pi \sin \theta/\lambda$) as obtained from the fitting of the XRD lines measured in the coatings deposited at $U_B = -40$ V (solid circles) and $U_B = -80$ V (open circles). The solid lines are the respective fits (the text provides more details).

linear Williamson–Hall dependence[38] is the partial coherence of nanocrystallites with small mutual misorientations. As explained in References 39 and 40, the partial coherence of nanocrystallites can be described by a partial overlap of the extremely broadened reciprocal lattice points from adjacent nanocrystallites. The overlapping reciprocal lattice points from these adjacent, partially coherent nanocrystallites get narrower, which is observed as a reduction of the XRD line broadening. The reduction of the XRD line broadening depends both on the distance between the partially coherent nanocrystallites and on the amount of the overlap of the reciprocal lattice points. Generally, the XRD line broadening increases with increasing diffraction vector, while the reciprocal lattice points from adjacent nanocrystallites overlap each other.[39,40] At high diffraction vectors, the overlap of the reciprocal lattice points disappears. Thus, the width of the XRD lines is not reduced, but remains constant. In this range of the diffraction vectors, the nanocrystallites appear in their true size for the XRD experiments. From the maximum line broadening (almost constant part of the line broadening in Figure 6), the crystallite sizes of (6.9 ± 0.5) nm and (4.0 ± 0.2) nm were calculated for the coatings deposited at $U_B = -40$ and -80 V, respectively.

B. *Lattice Strain in fcc-(Ti, Al) N Nanocrystallites*

In analogy with the classical theory of the XRD line broadening,[41,42] the extrapolation of the angular dependent (low-angle) part of the XRD line broadening to the zero diffraction vector, $q = 4\pi \sin \theta/\lambda = 0$, can be used for determination of the average size of clusters of partially coherent crystallites, as described in Reference 40. However, the extrapolated line broadening was equal to zero within experimental accuracy for the coatings under study. Therefore, it only can be said that the size of the clusters of partially coherent nanocrystallites exceeded the maximum size of the

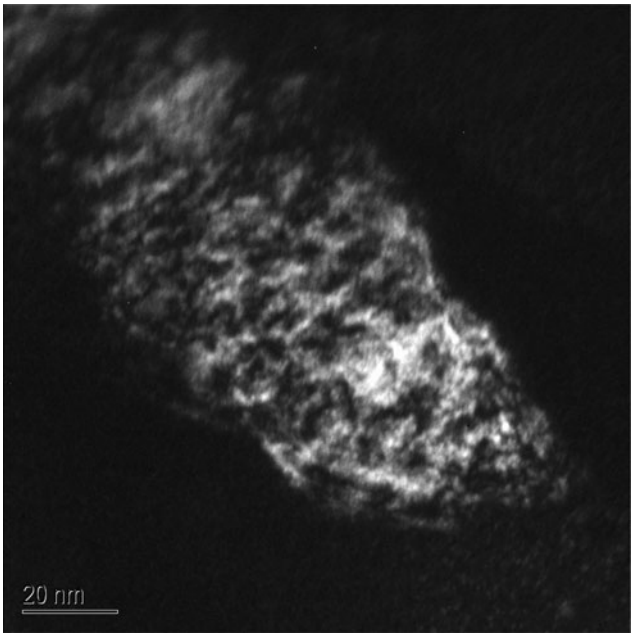

Fig. 7—TEM micrograph (dark-field mode) of one cluster of partially coherent crystallites from the CAE $Ti_{0.5}Al_{0.5}N$ coating deposited at $U_B = -80$ V. For this coating, GAXRD revealed the average crystallite size of ~4 nm.

objects accessible by XRD experiments. TEM in dark-field mode (Figure 7) revealed the cluster size over 100 nm. Furthermore, the transmission electron micrograph from Figure 7 confirms the existence of the nanocrystallites, which are visible *via* fragmentation of the cluster.

Whereas no significant difference in the cluster size was observed between the coatings deposited at different bias voltages, a large difference between the coatings was observed regarding the slopes of the line broadening at low diffraction vectors (Figure 6). The increase of the line width is much smaller in the coating deposited at $U_B = -40$ V than in the coating deposited at $U_B = -80$ V. The respective slopes of the plots are $(1.66 \pm 0.19) \times 10^{-3}$ and $(4.9 \pm 0.6) \times 10^{-3}$, which would correspond to the apparent microstrains of $(5.2 \pm 0.6) \times 10^{-3}$ and $(15.4 \pm 1.8) \times 10^{-3}$, as calculated using the Williamson-Hall method.[38] However, a direct classification of the origin of this apparent microstrain from the XRD line broadening is difficult, because the increase of the line broadening with increasing diffraction vector has at least two reasons. The first one is related to the different speeds of the decay of the partial coherence with increasing diffraction vector for crystallites having different kinds of mutual misorientation, because the slope of the dependence of the line broadening on the modulus of the diffraction vector (**q**) depends on the number of simultaneously coherent crystallites.[39] The more crystallites are simultaneously (partially) coherent, the lower is the increase of the line broadening with the diffraction vector. In general, many nanocrystallites are partially coherent if they are mutually "zigzag" misoriented; only a few nanocrystallites are partially coherent if their mutual misorientations accumulate over the distance.[40] As the line broadening is constant in the range of high diffraction vectors, the slope of the dependence of the line broadening on the modulus of the diffraction vector influences directly the height of a "jump" in the line broadening between the angular-dependent and the angular-independent parts (*cf.* Figure 6). The second possible reason for the additional broadening of XRD lines is an inhomogeneous variation of the interplanar spacing as caused by local lattice strains. These lattice strains can be caused by nonuniformly distributed aluminum atoms, by dislocations and dislocation structures,[19,43] and by the lattice misfit between fcc-(Ti, Al) N and w-AlN, as discussed previously.

C. *Thermally Activated Changes in the Microstructure of the Coatings*

Subsequently, the as-deposited samples were subjected to *in-situ* HT-GAXRD. The following differences in the microstructure of the CAE coatings deposited at $U_B = -40$ and $U_B = -80$ V were regarded as being important for the behavior of the coatings at high temperatures.

(1) The phase composition of the coatings: $Ti_{0.5}Al_{0.5}N$ deposited at $U_B = -40$ V contained a single crystalline phase, whereas $Ti_{0.5}Al_{0.5}N$ deposited at $U_B = -80$ V was a nanocomposite containing fcc-(Ti, Al) N and w-AlN with a strong mutual orientation relationship between the crystalline phases.
(2) The residual stress and the local lattice strain: the residual stress in the single-phase coating ($Ti_{0.5}Al_{0.5}N$ deposited at $U_B = -40$ V) was much lower than the residual stress in the dual-phase coating ($Ti_{0.5}Al_{0.5}N$ deposited at $U_B = -80$ V, Table I). The lattice misfit between fcc-(Ti, Al) N and w-AlN in the dual-phase coating is expected to generate additional local lattice strain at the phase boundaries.
(3) The crystallite size: the dual-phase coating contained smaller nanocrystallites than the single-phase coatings.

The dual-phase nature of the CAE $Ti_{0.5}Al_{0.5}N$ coatings deposited at $U_B = -80$ V together with the higher residual stress and the smaller crystallite size in the fcc phase were the reasons for the higher hardness of these coatings as compared with the coatings deposited at $U_B = -40$ V (Table I). In our former studies,[17–19] we observed analogous correlations between the microstructure parameters, *i.e.*, the increase of the residual stress and the reduction of the crystallite size in dual-phase coatings, for CAE (Ti, Al) N coatings with different aluminum contents that were deposited at the constant bias voltage of −75 V. Also in that case, the increase of the residual stress and the reduction of the crystallite size in dual-phase coatings led to the increase of the hardness.

The analysis of *in-situ* HT-GAXRD patterns was done concurrently using the line profile fitting and the Rietveld analysis. The most important parameters

obtained from the line profile fitting are the positions and integral breadths of diffraction lines. From these parameters, the stress-free lattice parameters, the macroscopic lattice strains, and the apparent microstrains were calculated using the approaches described in Sections A and B. The Rietveld analysis of the *in-situ* measured HT-GAXRD patterns was performed with the aid of the computer code MAUD.[44] The most important result of the Rietveld analysis was the information about the phase composition of the coatings during their thermal treatment. Furthermore, the Rietveld analysis using MAUD confirmed the results of the line profile fitting: the stress-free lattice parameters and the macroscopic lattice strains calculated using the alternative methods were identical within their experimental accuracy. The apparent microstrains were not compared as the model of partial coherence of neighboring crystallites is not implemented in MAUD.

The *in-situ* HT-GAXRD measurements have shown that the coating deposited at $U_B = -40$ V contains fcc-(Ti, Al) N as a single crystalline phase up to 933 K (660 °C) (Figure 8). The change of the stress-free lattice parameter of fcc-(Ti, Al) N (Figure 9) is caused by the thermal expansion in this temperature range. Still, the changes of the macroscopic (ε) and microscopic (e) lattice strains (Figure 9) indicate a change in the defect structure. In analogy to the results published in Reference 19, the concurrent increase of ε and decrease of e between the room temperature and 723 K (450 °C) can be explained by the movement of microstructural defects (*e.g.*, dislocations) and by the formation of networks of such defects. At 933 K (660 °C), the networks of defects responsible for the macroscopic lattice strain disbanded almost completely, as can be seen on the almost complete relaxation of the macroscopic lattice strain (Figure 9(b)). The cooling of the sample from 933 K (660 °C) to 383 K (110 °C) has no effect on the defect structure (Figures 9(b) and (c)), but only on the stress-free lattice parameter that decreased upon cooling (Figure 9(a)). However, the stress-free lattice parameter measured after cooling at 383 K (110 °C) is smaller than the stress-free lattice parameter measured in the as-deposited sample at 303 K (30 °C) (Figure 9(a)), although the thermal expansion should not play a role in this temperature range. A reason for this reduction of the size of the elementary cell can be the disappearance of point defects, *e.g.*, interstitial atoms, or a local rearrangement of Al atoms.

At 1158 K (885 °C), fcc-AlN and a small amount of w-AlN grew in the coating deposited at $U_B = -40$V at the expense of fcc-(Ti, Al) N (Figure 8). In the beginning, the phase segregation was accompanied by an increase of the microstrain (Figure 9(c)). In the course of the annealing, tensile stress developed in fcc-(Ti, Al) N at 1160 K (887 °C) (Figure 9(b)) in contrast to the

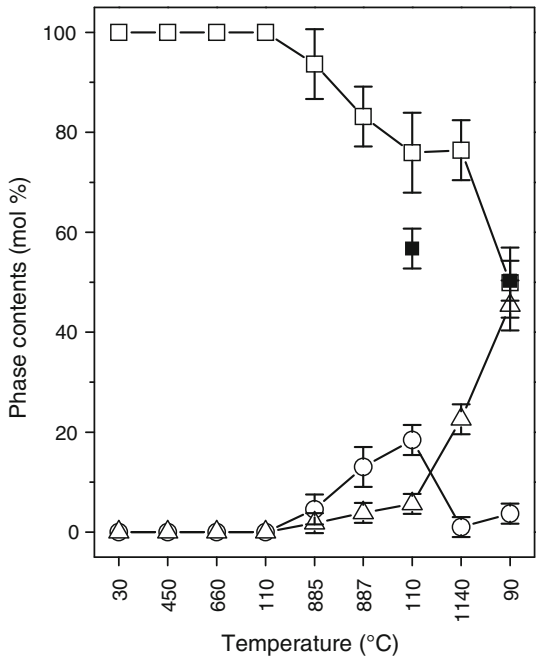

Fig. 8—Change of the phase composition as observed in the coating deposited at $U_B = -40$ V during its thermal treatment. Open symbols denote phase contents that were obtained using Rietveld analysis for fcc-(Ti, Al) N (boxes), fcc-AlN (circles), and w-AlN (triangles). Filled boxes stand for the fcc-(Ti, Al) N contents, which were calculated from the stress-free lattice parameters using Eq. [1], as described in Section III–A.

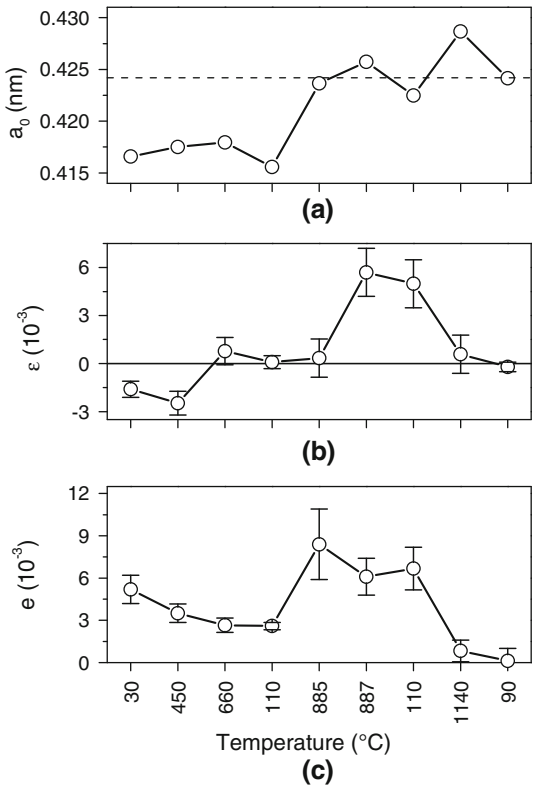

Fig. 9—Change of selected microstructural parameters during the thermal treatment as observed for the coating deposited at $U_B = -40$ V: (*a*) stress-free lattice parameter, (*b*) macroscopic lattice strain, and (*c*) apparent microstrain. For the stress-free lattice parameters, the error bars are smaller than the symbols. The dashed line in figure (a) marks the intrinsic lattice parameter of TiN (0.4242 nm).

compressive residual stress that was observed for this phase in the as-deposited sample (Table I). However, the tensile stress in fcc-(Ti, Al) N was compensated by a compressive stress in fcc-AlN; the corresponding "macroscopic" lattice strain in fcc-AlN was $\varepsilon = -(8 \pm 2) \times 10^{-3}$, as obtained from the *in-situ* HT-GAXRD experiment as well. The high stress-free (and thermal expansion free) lattice parameter measured in the coating cooled from 1160 K (887 °C) to 383 K (110 °C) (Figure 9(a)) indicates segregation of Al from fcc-(Ti, Al) N, which was necessary to build fcc-AlN and w-AlN (Figure 8). According to the stress-free lattice parameter (Figure 9(a)), the coating contains after cooling from 1160 K (887 °C) to 383 K (110 °C) approximately 43 mol pct aluminum nitrides (fcc-AlN and w-AlN) as complementary phases to fcc-(Ti, Al) N (compare Figure 8). The discrepancy between the phase composition as calculated from the intensities of the diffraction lines (open symbols in Figure 8) and the contents of fcc-(Ti, Al) N as obtained from the stress-free lattice parameter (solid box in Figure 8) at 383 K (110 °C) indicates that some aluminum atoms are located outside the crystalline phases or outside the regular lattice sites. Such atoms act as structure defects that raise the lattice strains (Figures 9(b) and (c)). Further heating to 1413 K (1140 °C) and the final cooling to 363 K (90 °C) led to a further phase decomposition (Figure 8) and to the relaxation of the macroscopic and microscopic lattice strains (Figures 9(b) and (c)). The second dominant crystalline phase was w-AlN. At the end of the thermal treatment, the coating consisted of 50 mol pct fcc-TiN, which contained no Al, as confirmed by the stress-free lattice parameter, and nearly 50 mol pct w-AlN.

The high-temperature behavior of the CAE $Ti_{0.5}Al_{0.5}N$ coatings deposited at $U_B = -80$ V differs significantly from the high-temperature behavior of the coatings deposited at $U_B = -40$ V (compare Figures 8 through 11). The increase of the stress-free lattice parameter with increasing temperature up to 933 K (660 °C) is lower than expected solely for the thermal expansion, which was estimated from the change of the stress-free lattice parameter in the single-phase coating (Figure 9(a)). On the contrary, the decrease of the stress-free lattice parameter upon cooling from 933 K (660 °C) to 393 K (120 °C) is high (Figure 11(a)). Thus, the stress-free lattice parameter at 393 K (120 °C) is significantly lower than the stress-free lattice parameter measured in the as-deposited sample at 294 K (21 °C). Both phenomena indicate that aluminum is incorporated into the crystal structure of fcc-(Ti, Al) N in the temperature range up to 933 K (660 °C). Assuming that this aluminum comes from aluminum nitrides present in the as-deposited sample (approximately 28 mol pct; Section A), the amount of fcc-(Ti, Al) N in the coating deposited at $U_B = -80$ V would increase from (72 ± 2) mol pct in the as-deposited state to (90 ± 4) mol pct after heating to 933 K (660 °C) and cooling to 393 K (120 °C) (filled symbols in Figure 10). As no diffraction lines from w-AlN were observed in the HT-GAXRD diffraction patterns up to 933 K (660 °C), we suppose that w-AlN grows hetero-epitaxially on fcc-(Ti, Al) N

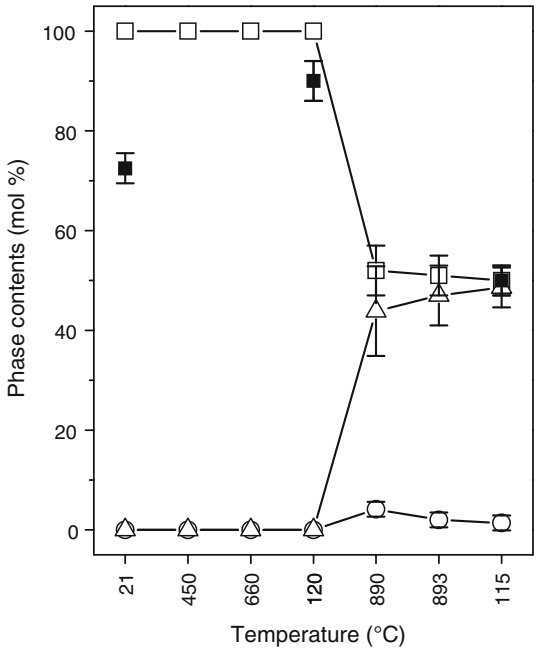

Fig. 10—Change of the phase composition as observed in the coating deposited at $U_B = -80$ V during its thermal treatment. The meaning of the symbols is the same as in Fig. 8.

between room temperature and 933 K (660 °C), as was described in Section A. The integration of aluminum into the crystal structure of fcc-(Ti, Al) N runs simultaneously with the diffusion of other microstructure defects. As for the coating deposited at $U_B = -40$ V, the increase of the macroscopic lattice strain between the room temperature and 723 K (450 °C) observed in the coating deposited at $U_B = -80$ V (Figure 11(b)) can be explained by the formation of defect networks during the movement of the microstructure defects. The incorporation of Al into the crystal structure of fcc-(Ti, Al) N is probably responsible for the slight increase of the local (microscopic) lattice strain between the room temperature and 723 K (450 °C) (Figure 11(c)). Temperatures over 723 K (450 °C) lead to the relaxation of macroscopic and microscopic lattice strains (Figures 11(b) and (c)). A temporary increase of the macroscopic lattice strain was only observed in conjunction with the decomposition of the coating into fcc-TiN and w-AlN above 1163 K (890 °C) (compare Figures 10 and 11(b)). As the amount of fcc-AlN was negligible in this case (Figure 10), the residual stress in fcc-(Ti, Al) N was compressive.

IV. DISCUSSION

The preceding results (Section III–C) showed clearly the influence of the microstructure of the cathodic arc evaporated nanocrystalline coatings with the chemical composition $Ti_{0.5}Al_{0.5}N$ on their thermal stability. In this study, the microstructure of the coatings was controlled solely by the bias voltage. The $Ti_{0.5}Al_{0.5}N$ coatings deposited at a lower bias voltage ($U_B = -40$ V) contained only one nanocrystalline phase, *i.e.*, fcc-(Ti, Al)

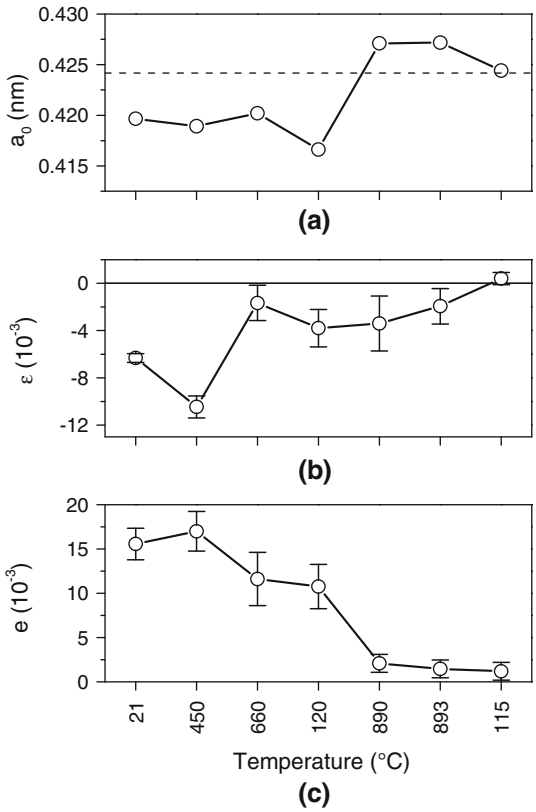

Fig. 11—Change of selected microstructure parameters during the thermal treatment as observed for the coating deposited at $U_B = -80$ V: (*a*) stress-free lattice parameter, (*b*) macroscopic lattice strain, and (*c*) apparent microstrain. For the stress-free lattice parameters, the size of the error bars is comparable with the size of the symbols. The dashed line in (a) marks the intrinsic lattice parameter of TiN (0.4242 nm).

N, that was under a low intrinsic compressive residual stress. In the $Ti_{0.5}Al_{0.5}N$ coatings deposited at a higher bias voltage ($U_B = -80$ V), nanocrystalline w-AlN was found as a minor crystalline phase that grew with a strong orientation relationship to the dominant fcc-(Ti, Al) N. The presence of w-AlN in the coatings led to a considerable increase of the lattice strains. Both the macroscopic and the microscopic lattice strains increased about 3 times, when the bias voltage was increased from −40 to −80 V. Furthermore, the increase of the bias voltage caused a reduction of the crystallite size by more than 40 pct. The presence of a second phase and the smaller crystallite size in the $Ti_{0.5}Al_{0.5}N$ coatings deposited at $U_B = -80$ V are two phenomena that indicate a limited mobility of the deposited atoms. The limited mobility of the metallic atoms affects directly their distribution in the coatings, as illustrated in Reference 45. The nonuniform distribution of Ti and Al in the (Ti, Al) N coatings leads to a "fragmentation" of the deposited coatings (Figure 7) and to the development of lattice strains (Table I; Figures 3, 6, 9, and 11).

As shown in Section III–A, the lattice misfit between fcc-(Ti, Al) N and w-AlN or fcc-AlN can be regarded as a very important additional source of the lattice strain, which accompanies the intrinsic lattice strain that is usually observed in the single-phase coatings. The lattice misfit at the fcc-(Ti, Al) N/w-AlN interface, which was calculated according to Eqs. [6] and [7] for the observed orientation relationship, causes lattice expansion in fcc-(Ti, Al) N and lattice contraction in w-AlN. The expected lattice strains change considerably if aluminum nitride is present in its cubic modification. Assuming that fcc-(Ti, Al) N and fcc-AlN have the same local crystallographic orientation at their interface,[28,46] the difference of their lattice parameters leads to a lattice misfit, which causes lattice contraction in fcc-(Ti, Al) N and lattice expansion in fcc-AlN. In samples consisting of fcc-(Ti, Al) N and w-AlN with a strong mutual orientation relationship, *i.e.*, in $Ti_{0.5}Al_{0.5}N$ deposited at $U_B = -80$ V and heated to 723 K (450 °C), considerable compressive residual stress in fcc-(Ti, Al) N was observed. In samples containing coherent fcc-(Ti, Al) N and fcc-AlN, *i.e.*, in $Ti_{0.5}Al_{0.5}N$ deposited at $U_B = -40$ V and heated to 1158 K (885 °C), fcc-(Ti, Al) was under tensile stress and fcc-AlN under compressive stress.

The presence of macroscopic residual stresses indicates a strong dependence of the mechanical interaction between the phases at their interfaces on the macroscopic direction. A possible interpretation of this experimental result is that the fcc-(Ti, Al) N/w-AlN or the fcc-(Ti, Al) N/fcc-AlN interfaces grow perpendicularly to the substrate. Such a growth would be a plausible consequence of the limited surface mobility of the atoms during the deposition process discussed previously. For the fcc-(Ti, Al) N/w-AlN interfaces laying perpendicular to the sample surface, the lattice expansion in fcc-(Ti, Al) N would reach its maximum in the sample surface perpendicular direction, which is interpreted as compressive residual stress within the $\sin^2\psi$ method (Section III–A). For the same reason, the lattice compression in fcc-(Ti, Al) N and the lattice expansion in fcc-AlN at their interfaces look like tensile stress in fcc-(Ti, Al) N and compressive stress in fcc-AlN, respectively, if the interfaces lie perpendicular to the substrate.

The lattice strains, which arise at the phase boundaries and in the vicinity of other microstructural defects, affect seriously the hardness of the (Ti, Al) N coatings at high temperatures. The temperature dependence of the hardness of the (Ti, Al) N coatings is usually measured *ex situ* on annealed samples and is shown for two limit cases (*e.g.*, References 5, 6, 12, and 16), *i.e.*, for nonoptimized TiN coatings, in which the hardness decreases steadily above approximately 673 K (400 °C), and for optimized coatings such as $Ti_{0.34}Al_{0.66}N$, in which the hardness shows a maximum between 1073 K (800 °C) and 1223 K (950 °C). Our results obtained on the $Ti_{0.5}Al_{0.5}N$ coatings deposited at $U_B = -40$ V confirm that the hardness maximum at high temperatures is related to the formation of the fcc-(Ti, Al) N/fcc-AlN nanocomposites with coherent interfaces between fcc-(Ti, Al) N and fcc-AlN nanocrystallites. The lattice misfit at these interfaces is an important source of lattice strains, which are responsible for enhancement of the hardness of the coatings.

The comparison of the macroscopic and microscopic strains with the amount of fcc-AlN in the coating deposited at $U_B = -40$ V shows a slight delay of the increase of the macroscopic strain (ε from Figure 9(b))

at ~1158 K (885 °C) in comparison with the amount of fcc-AlN (Figure 8) and with the increase of the microscopic strain (*e* from Figure 9(c)). This phenomenon can be explained by a gradual rearrangement of Al atoms. At the beginning, the rearrangement of Al atoms is visible as microstrain only, because the diffusing Al atoms behave almost like lattice defects. Thus, they cause the apparent local lattice strain. A part of the Al atoms forms fcc-AlN, but it is still not visible directly in the XRD patterns for a similar reason that was discussed previously for w-AlN (Section III–A). Later on, the volume of fcc-AlN and the difference in the lattice parameters of fcc-AlN and fcc-(Ti, Al) N becomes sufficient to be seen by XRD (Figure 8). A further growth of fcc-AlN is responsible for the observed increase of the macroscopic lattice strain. The heating of the samples to 1413 K (1140 °C) led to the formation of w-AlN instead of fcc-AlN, to the transformation of fcc-AlN into w-AlN, to a further out-diffusion of Al from fcc-(Ti, Al) N, and to a full relaxation of the lattice strains (Figure 9). The consequence of these processes is a rapid decrease of the hardness of the coatings, as reported in the literature.

In a similar manner, the changes of the microstructure parameters can be discussed for the CAE $Ti_{0.5}Al_{0.5}N$ coatings deposited at $U_B = -80$ V. As controlled by the high macroscopic and microscopic lattice strains (Figure 11) caused by the presence of w-AlN (Figures 4 and 5), the hardness of such fcc-(Ti, Al) N/w-AlN nanocomposites in the as-deposited state is quite high (Table I). As the lattice strains increase at 723 K (450 °C) (Figure 11), even a further increase of the hardness in this temperature region is expected. However, a further increase of the temperature leads to a temporary incorporation of Al atoms (probably from w-AlN) into fcc-(Ti, Al) N (Figure 11(a) and the solid boxes in Figure 10) and to a gradual relaxation of the lattice strains (Figures 11(b) and (c)). Only a very low amount of fcc-AlN was observed at 1163 K (890 °C) (Figure 10), as this phase transformed into w-AlN very quickly. Also, the out-diffusion of Al from fcc-(Ti, Al) N was very fast. Already at 1163 K (890 °C), the decomposition of fcc-(Ti, Al) N into fcc-TiN and w-AlN was nearly completed (Figure 10). A typical consequence of these processes is a decrease of the hardness already at medium temperatures.

The preceding correlation between the presence of fcc-AlN, the increase of the residual stresses, and the local lattice strains can also be discussed from the point of view of the interplay between the lattice misfit at the fcc-(Ti, Al) N/w-AlN or fcc-(Ti, Al) N/fcc-AlN interfaces and the diffusion kinetics. As follows from Eqs. [1], [6], and [7], the lattice misfit between fcc-$Ti_{1-x}Al_xN$ and w-AlN decreases with decreasing Al contents in fcc-(Ti, Al) N. Consequently, the out-diffusion of Al from fcc-(Ti, Al) N and the decomposition of fcc-(Ti, Al) N into fcc-TiN and w-AlN are assumed to be accelerated at the fcc-(Ti, Al) N/w-AlN interfaces, because the separation of elements reduces the lattice misfit between fcc-(Ti, Al) N and w-AlN. On the contrary, the out-diffusion of Al from fcc-(Ti, Al) N into fcc-AlN (at the fcc-(Ti, Al) N/fcc-AlN interfaces) is assumed to be retarded, as the reduction of aluminum contents in fcc-(Ti, Al) N would increase the lattice misfit between fcc-(Ti, Al) N and fcc-AlN. These assumptions were confirmed experimentally. The dual-phase $Ti_{0.5}Al_{0.5}N$ coatings containing w-AlN in the as-deposited state decomposed earlier than the single-phase coatings containing only fcc-(Ti, Al) N. Particularly, the temperature-induced growth of fcc-AlN in originally single-phase coatings seems to delay the decomposition of fcc-(Ti, Al) N into fcc-TiN and w-AlN.

V. CONCLUSIONS

Based on the results of detailed microstructural analysis, we explained how the microstructure of the CAE $Ti_{0.5}Al_{0.5}N$ coatings deposited at different bias voltages influences their hardness and thermal stability. The bias voltage was found to affect the mobility of the metallic atoms during the deposition process and, consequently, their distribution in the as-deposited samples. The increase of the bias voltage from −40 to −80 V decreased the mobility of the atoms and increased the local fluctuations in the concentration of the metallic species. In general, such local fluctuations of the chemical composition in the coatings were identified as a reason for the formation of local lattice strains (microstrains) and as an origin of the phase segregation. One consequence of the limited mobility of the deposited atoms at $U_B = -80$ V was the presence of w-AlN as a second crystalline phase in the CAE $Ti_{0.5}Al_{0.5}N$ coatings. As the irregular distribution of the metallic atoms is one of the phenomena that are responsible for the formation of lattice strains, it improves the hardness of the coatings at low and medium temperatures. On the contrary, a highly irregular distribution of the atoms promotes the formation of AlN with the wurtzitic crystal structure, the presence of which accelerates the decomposition of fcc-(Ti, Al) N into fcc-TiN and w-AlN, the relaxation of the lattice strains, and finally the degradation of the hardness at high temperatures.

ACKNOWLEDGMENTS

This work was performed within the Cluster of Excellence "Structure Design of Novel High-Performance Materials via Atomic Design and Defect Engineering (ADDE)" that is financially supported by the European Union and by the Ministry of Science and Art of Saxony (SMWK). Furthermore, we acknowledge the financial support of Project No. RA-1050/9 through the German Research Foundation (DFG).

REFERENCES

1. V. Derflinger, H. Brändle, and H. Zimmermann: *Surf. Coat. Technol.*, 1999, vol. 113, pp. 286–92.
2. D. McIntyre, J.E. Greene, G. Håkansson, J.-E. Sundgren, and W.-D. Münz: *J. Appl. Phys.*, 1990, vol. 67, pp. 1542–53.
3. P.H. Mayrhofer, C. Mitterer, L. Hultman, and H. Clemens: *Prog. Mater. Sci.*, 2006, vol. 51, pp. 1032–1114.

4. Y.C. Chim, X.Z. Ding, X.T. Zeng, and S. Zhang: *Thin Solid Films*, 2009, vol. 517, pp. 4845–49.
5. A. Hörling, L. Hultman, M. Odén, J. Sjölén, and L. Karlsson: *Surf. Coat. Technol.*, 2005, vol. 191, pp. 384–92.
6. S. Veprek, M.G.J. Veprek-Heijman, P. Karvankova, and J. Prochazka: *Thin Solid Films*, 2005, vol. 476, pp. 1–29.
7. H. Oettel, R. Wiedemann, and S. Preissler: *Surf. Coat. Technol.*, 1995, vol. 74, pp. 273–78.
8. W. Herr and E. Broszeit: *Surf. Coat. Technol.*, 1997, vol. 97, pp. 335–40.
9. L. Hultman: *Vacuum*, 2000, vol. 57, pp. 1–30.
10. C.-M. Suh, B.-W. Hwang, and R.-I. Murakami: *Mater. Sci. Eng. A*, 2003, vol. 343, pp. 1–7.
11. A. Hörling, L. Hultman, M. Odén, J. Sjölén, and L. Karlsson: *J. Vac. Sci. Technol. A*, 2002, vol. 20, pp. 1815–23.
12. P.H. Mayrhofer, A. Hörling, L. Karlsson, J. Sjölén, C. Mitterer, and L. Hultman: *Appl. Phys. Lett.*, 2003, vol. 83, pp. 2049–51.
13. P.H. Mayrhofer, C. Mitterer, and J. Musil: *Surf. Coat. Technol.*, 2003, vols. 174–175, pp. 725–31.
14. E.O. Hall: *Proc. Phys. Soc. London Sect. B*, 1951, vol. 64, pp. 747–49.
15. N.J. Petch: *J. Iron Steel Inst.*, 1953, vol. 174, pp. 25–28.
16. S. Veprek, H.-D. Männling, M. Jílek, and P. Holubář: *Mater. Sci. Eng. A*, 2004, vol. 366, pp. 202–05.
17. D. Rafaja, A. Poklad, V. Klemm, G. Schreiber, D. Heger, M. Šíma, and M. Dopita: *Thin Solid Films*, 2006, vol. 514, pp. 240–49.
18. D. Rafaja, A. Poklad, V. Klemm, G. Schreiber, D. Heger, and M. Šíma: *Mater. Sci. Eng. A*, 2007, vol. 462, pp. 279–82.
19. D. Rafaja, C. Wüstefeld, M. Dopita, V. Klemm, D. Heger, G. Schreiber, and M. Šíma: *Surf. Coat. Technol.*, 2008, vol. 203, pp. 572–78.
20. H.W. Hugosson, H. Högberg, M. Algren, M. Rodmar, and T.I. Selinder: *J. Appl. Phys.*, 2003, vol. 93, pp. 4505–11.
21. K. Kutschej, P.H. Mayrhofer, M. Kathrein, P. Polcik, R. Tessadri, and C. Mitterer: *Surf. Coat. Technol.*, 2005, vol. 200, pp. 2358–65.
22. P.H. Mayrhofer, D. Music, and J.M. Schneider: *Appl. Phys. Lett.,* 2006, vol. 88, paper no. 071922.
23. S. PalDey and S.C. Deevi: *Mater. Sci. Eng. A*, 2002, vol. 342, pp. 58–79.
24. M. Pfeiler, K. Kutschej, M. Penoy, C. Michotte, C. Mitterer, and M. Kathrein: *Surf. Coat. Technol.*, 2007, vol. 202, pp. 1050–54.
25. M. Pfeiler, G.A. Fontalvo, J. Wagner, K. Kutschej, M. Penoy, C. Michotte, C. Mitterer, and M. Kathrein: *Tribol. Lett.*, 2008, vol. 30, pp. 91–97.
26. P.H. Mayrhofer, D. Music, and J.M. Schneider: *J. Appl. Phys.,* 2006, vol. 100, paper no. 094906.
27. A. Navrotsky: *J. Chem. Thermodyn.*, 2007, vol. 39, pp. 1–9.
28. P.H. Mayrhofer, F.D. Fischer, H.J. Böhm, C. Mitterer, and J.M. Schneider: *Acta Mater.*, 2007, vol. 55, pp. 1441–46.
29. F. Adibi, I. Petrov, L. Hultman, U. Wahlström, T. Shimizu, D. McIntyre, J.E. Greene, and J.-E. Sundgren: *J. Appl. Phys.*, 1991, vol. 69, pp. 6437–50.
30. O. Durand-Drouhin, A.E. Santana, A. Karimi, V.H. Derflinger, and A. Schütze: *Surf. Coat. Technol.*, 2003, vols. 163–164, pp. 260–66.
31. A.E. Santana, A. Karimi, V.H. Derflinger, and A. Schütze: *Surf. Coat. Technol.*, 2004, vols. 177–178, pp. 334–40.
32. Inorganic Crystal Structure Database, ICSD on CD-ROM, FIZ Karlsruhe and NIST Gaithersburg, version 2009-2.
33. A.J. Perry, V. Valvoda, and D. Rafaja: *Thin Solid Films*, 1992, vol. 214, pp. 169–74.
34. D. Rafaja, M. Dopita, M. Růžička, V. Klemm, D. Heger, G. Schreiber, and M. Šíma: *Surf. Coat. Technol.*, 2006, vol. 201, pp. 2835–43.
35. M. Dopita, D. Rafaja, C. Wüstefeld, M. Růžička, V. Klemm, D. Heger, G. Schreiber, and M. Šíma: *Surf. Coat. Technol.*, 2008, vol. 202, pp. 3199–3207.
36. C. Kral, W. Lengauer, D. Rafaja, and P. Ettmayer: *J. Alloys Compd.*, 1998, vol. 265, pp. 215–33.
37. D. Rafaja, V. Valvoda, R. Kužel, A.J. Perry, and J.R. Treglio: *Surf. Coat. Technol.*, 1996, vols. 86–87, pp. 302–08.
38. G.K. Williamson and A.H. Hall: *Acta Metall. Mater.*, 1953, vol. 1, pp. 22–31.
39. D. Rafaja, V. Klemm, G. Schreiber, M. Knapp, and R. Kužel: *J. Appl. Cryst.*, 2004, vol. 37, pp. 613–20.
40. D. Rafaja, V. Klemm, C. Wüstefeld, M. Motylenko, M. Dopita, M. Schwarz, T. Barsukova, and E. Kroke: *Z. Kristallogr. Suppl.*, 2008, vol. 27, pp. 15–26.
41. B.E. Warren: *X-ray Diffraction*, Dover, New York, NY, 1990.
42. M.A. Krivoglaz: *X-Ray and Neutron Diffraction in Non-Ideal Crystals*, Springer, Berlin, 1996.
43. D. Rafaja, Ch. Wüstefeld, M. Dopita, M. Růžička, V. Klemm, G. Schreiber, D. Heger, and M. Šíma: *Surf. Coat. Technol.*, 2007, vol. 201, pp. 9476–84.
44. L. Lutterotti, D. Chateigner, S. Ferrari, and J. Ricote: *Thin Solid Films*, 2004, vol. 450, pp. 34–41.
45. R. Rachbauer, E. Stergar, S. Massl, M. Moser, and P.H. Mayrhofer: *Scripta Mater.*, 2009, vol. 61, pp. 725–28.
46. D. Rafaja, M. Šíma, V. Klemm, G. Schreiber, D. Heger, L. Havela, and R. Kužel: *J. Alloys Compd.*, 2004, vol. 378, pp. 107–11.